Authors Version

Oxidation behavior of Nb-coated Zirconium Diboride

J. E. Förster^a, R. Naraparaju^a, W.G. Fahrenholtz^b and G.E. Hilmas^b

Journal of the European Ceramic Society

https://doi.org/10.1016/j.jeurceramsoc.2023.04.029

^a Institute of Materials Research, DLR - German Aerospace Center, Cologne, Germany

^b Department of Materials, Science and Engineering, Missouri University of Science & Technology, Rolla, MO, United States

Oxidation behavior of Nb-coated Zirconium Diboride

J. E. Förster^a, R. Naraparaju^a, W.G. Fahrenholtz^b and G.E. Hilmas^b

Abstract

Metallic Nb-coatings were deposited on top of ZrB₂ by means of magnetron sputtering to improve its oxidation resistance. High temperature oxidation tests have revealed that the metallic Nb-coatings have shown promising results by forming a dense solid and protective reaction zone in addition to a more stable B₂O₃ liquid solution at the surface. Compared to baseline ZrB₂, a reduction in the oxidation kinetics, as well as the thickness of the porous zirconia layer by 76 %, has been achieved with the help of Nb-coatings. It was determined that a "liquid phase sintering by molten Nb₂O₅"mechanism was mainly guiding the formation of the dense reaction zone under the boria layer, resulting in the improved oxidation resistance. Furthermore, the experiments revealed the need for an annealing process of Nb-coated specimens, in vacuum, to improve the adhesion of the coatings with ZrB₂ and to avoid spallation during oxidation.

1 | Introduction

The demand for more efficient materials at elevated temperatures is ever-increasing and the availability of such materials is scarce. ZrB₂ is a member of the family of Ultra-High Temperature Ceramics (UHTCs) and has unique properties like a melting temperature of 3240 °C, a theoretical density of 6.085 g/cm³, and thermal conductivity of 75 W/m-K at 2000°C, which makes it very attractive for applications in hypersonic vehicles [1-4]. Previous studies on ZrB₂ have recognized distinct oxidation behavior under three temperature regimes: At temperatures < 1000 °C, the oxidation rate of ZrB₂ is assumed to be parabolic due to the formation of crystalline zirconia (ZrO₂) and a continuous liquid layer of boria (B₂O₃). By reducing the oxygen diffusion to the reaction front, B₂O₃ provides passive protection against further oxidation and leads to parabolic oxidation kinetics. At temperatures between 1000 °C and 1800 °C, the mass gain due to the formation of ZrO₂ and B₂O₃, as well as the mass loss due to the evaporation of B₂O₃, leads to para-linear oxidation kinetics. Above 1800 °C, B₂O₃ starts to evaporate immediately at the reaction front of ZrB₂ and no protective glassy layer forms [5-7]. However, the low oxidation resistance in oxidative atmospheres above 1400 °C limits its usability and is a drawback for hypersonic applications like thermal protective systems, flight stabilizing parts, and components

^a Institute of Materials Research, DLR - German Aerospace Center, Cologne, Germany

^b Department of Materials, Science and Engineering, Missouri University of Science & Technology, Rolla, MO, United States

in scramjet engines [8]. Several studies have examined the effect of transition metals such as W, Nb, or Mo on the oxidation behavior of ZrB₂. Oxidation products of corresponding elements were soluble in ZrO₂ and enabled the formation of solid solutions, which are stable at elevated temperatures. Zhang et al reported the beneficial effect of the addition of 4 mol% tungsten carbide by forming WO₃ inside the oxide scale. The liquid WO₃ promoted liquid phase sintering of the porous zirconia and the densification of the oxide scale. Studies of Dedashtie et al have proven, that the addition of 6 mol% pure W or Nb to ZrB₂ leads to the formation of a porous oxide layer containing zirconia and solid solutions. Simultaneously, the additions increased the stability of the protective glassy boria scale at the surface, which improved the oxidation behavior compared to baseline ZrB₂ [9-13]. It is known, that Nb₂O₅ is soluble in ZrO₂ and B₂O₃ above 1420°C. A surplus of Nb₂O₅ might result in the formation of a more stable Nb₂O₅-containing boria glass, a zirconia-based solid solution, and a niobia-rich liquid solution [14-18]. The latter could promote densification due to liquid phase sintering, compared to the addition of tungsten carbide [15, 16, 19, 20]. Therefore, Nb was applied as an overlay coating on top of ZrB₂, to improve the oxidation resistance of baseline ZrB₂, expecting that the concentration gradient between ZrB₂ and Nb at the interface zone, and the consequential reaction of niobia and zirconia, will change the oxidation behavior.

2 | EXPERIMENTAL METHOD

This study used baseline ZrB₂ specimens with a relative density of >95 % and an average grain size of 19±13 µm. The specimens were prepared by hot pressing at 2100 °C from commercial powders (Grade B, H.C. Starck, Newton, MA) with a purity of 98.2 % and Hf impurity of 1.9 wt%. Details of the processing methods and microstructure analysis are described elsewhere [21]. Specimens were cut by electrical discharge machining (EDM) into eqi-sized rectangles with a size of 13.0 mm x 6.5 mm x 3.0 mm and an average weight of 1.5 g (AGIECUT 150 HSS, 0.3 mm wire, copper). The top-sides of the specimens were mirror-polished with general metallographic preparation methods and ultrasonically cleaned in deionized water. Nb coatings with a thickness of 8.8±0.8 µm were applied by means of magnetron sputtering method (Z400, Systec Vacuum Coating, Karlstadt, Germany). Coated specimens were annealed in vacuum with a heating rate of 5 °C/min specimens until 1500 °C, followed by a heating rate of 1 °C/min to 1800 °C. Subsequently, the temperature was held for 1h at 1800 °C, and then cooled rapidly to 1750 °C and held for 3h. Afterwards, specimens were cooled to room temperature with a rate of 5 °C/min. Table 1 shows the nomenclature of the tested specimens and corresponding information about the experimental conditions. The oxidation experiments were performed in a tube furnace (Nabertherm, RHTH 120/300/16, Germany), equipped with an Al₂O₃-tube.

Specimens rested on top of alumina powder (Nabolax No 625-31) poured into an alumina crucible to avoid the possibility of sticking to the crucible. Specimens were placed in the center of the furnace to ensure consistent temperature conditions. The furnace was initially flushed with synthetic air (SA). Afterwards, a constant flowrate of SA was set to 0.4 L/min (corresponds to a linear flow rate of 0.3 cm/s, based on the tube diameter of 55 mm). The furnace was heated at 10 °C/min to 1500 °C, held for 1h or 4h at peak temperature, and cooled down at 10 °C/min to room temperature. Scanning electron microscopy (SEM), equipped with a back-scatter-electron detector (BSE) was used to analyze the oxidized specimens (DSM Ultra 55, Carl Zeiss NTS, Wetzlar, Germany). High resolution images of oxidized top-sides were taken, stitched together, and analyzed by means of image processing software (ImageJ, National Institutes of Health, Bethesda, MD) to calculate the coverage of boria glass on the oxidized surfaces. Specimens were cut from the backside with a wire cut saw (Precision diamond wire saw 3242, Well Diamond Wire Saw SA, Germany; wire diameter 0.3 mm) to create a clean determined fracturing point. The thicknesses of the oxide scales and glassy B₂O₃-layer were measured on fractured surfaces. Specimens were mounted in conductive epoxy and polished to a surface finish of 0.25 µm using standard metallographic methods. Polished cross-sections were used to measure the thickness of single sub-layers in the oxide scale. Thicknesses were always measured in the center regions of specimens. The porosity was calculated using high resolution images of polished cross sections and the use of the common particle measurement function of ImageJ. SEM was equipped with energy-dispersive X-ray spectroscopy (EDS), which was used to measure the interdiffusion depth after annealing and the infiltration of Nb after oxidation (Inca, Oxford Instruments Abingdon, UK). Crystalline phases of the oxide scale were measured by means of X-ray diffraction (XRD). The XRD measurements were performed with a Co-radiation source (Siemens D5000 diffractometer) and analyzed subsequently (EVA/Topas 4.2 software package, Bruker AXS Karlsruhe, Germany). Transmission electron microscopy (TEM) was used to identify the different crystal structures inside the oxide scale via diffractograms (ICCD2019 database). The lamella was sliced by focused ion beam (FIB).

3 | RESULTS

3.1 | AS-COATED SPECIMENS

An Al₂O₃ substrate was coated, in addition to the ZrB₂ specimens, and was only used to inspect the deposited Nb-coating. The BSE cross-section of the Nb-coated Al₂O₃ substrate shown in Fig. 1a confirms a uniform Nb-coating with a thickness of 8.8±0.8 μm exhibiting characteristic columnar grains. This condition was defined as "As-coated" (AC). Fig. 1b-d show BSE

micrographs of oxidized surfaces of AC after 1h of oxidation (AC1) as well as the B_2O_3 -scale via fractured surfaces. A continuous layer of boria was identified, which covered the surface by ~52 %. The residual area was covered by arbitrary grains with an average size of $28.2\pm9.7~\mu m$ (Fig. 1b). According to EDS spot-analysis (not in the report), engraved micro structured areas on top of the arbitrary grains consisted of zirconia and traces of niobium (Fig. 1c). Fractured surfaces showed a maximum B_2O_3 -layer thickness of $33.5~\mu m$. Aciculate Nb-oxide particles were present inside the glassy layer (Fig. 1d). X-ray diffraction was used to characterize the phases on oxidized surfaces of AC1 specimens. Monoclinic ZrO_2 , triclinic H_3BO_3 , and orthorhombic $Nb_2Zr_6O_{17}$ were detected (PDF card numbers 37-1484, 30-0199, and 09-0251).

3.2 | ANNEALED NB-COATED SPECIMENS

Darkfield light microscopy was used to identify defects on the surface after the annealing procedure. No spallation, cracks, or other defects were observed. BSE cross-sections of annealed specimens are presented in Fig. 2. The cross-sectional micrographs revealed a porosity of 5.8 % in the interface zone. The thickness of the coating did not change during the annealing process (~8.8 µm) (Fig. 2a). EDS line-scans were used to identify the chemical composition in the interface zone. The scans indicated the formation of a homogeneous interdiffusion zone (IDZ) between the Nb-coating and ZrB₂. The average thickness of the IDZ was 3.4 µm (Fig. 2b). This condition is defined as "Annealed" (AN). Fig. 3 shows the surface conditions after oxidation. After 1h at 1500 °C (AN1) the annealed specimens appeared blackish. ~99 % of the coated surface was covered by B₂O₃ after oxidation (Fig. 3a). Globular grains of ZrO₂ were sparsely distributed on top of the covered surface. The globular grains showed a smooth surface and had an average size of 5.0±1.4 µm (Fig. 3b). Fractured cross-section revealed an intact B₂O₃-layer (~36 μm thick). No grains or other particles were found inside the glassy layer (Fig. 3c). After 4h of oxidation at 1500°C (AN4), the surfaces of annealed specimens were still covered with boria glass and appeared dark brownish in the center. A total coverage of ~62 % by glassy boria (~69 µm thick) was calculated with the help of BSE micrographs (Fig. 3d). Zirconia grains on top of the glass had an average size of 6.7±1.8 µm with a smooth surface and engraved areas of a Nbrich phase (Fig. 3e). Arbitrary shaped grains of zirconia and niobia were detected by EDS spotanalysis in the interface of the solid and glassy oxide layer (Fig. 3f). X-ray diffraction patterns from the surfaces of AN1 and AN4 specimens are shown in Fig. 4. Monoclinic ZrO₂, orthorhombic B₅H₁₂NO₁₂, and orthorhombic Nb₂Zr₆O₁₇ were detected for all the annealed specimens after oxidation (PDF card numbers 36-0420, 31-0043, and 09-0251).

3.3 | OXIDE SCALE MORPHOLOGY AFTER OXIDATION AT 1500 °C

Fig. 5 presents BSE cross sections of AC1, AN1 and AN4. Compared to baseline ZrB₂, Nb-coated specimens always formed a multilayer oxide scale, which consisted of a mixed oxide zone (MZ), a dense oxide zone (DZ), and a porous oxide zone (PZ). Each zone was analyzed by EDS spotanalysis and presented in Fig. 6. The PZ of oxidized specimens consisted of pure ZrO₂ (Spec. 5) with a porosity of 7.0±3.8 %, 7.1±3.1 %, and 6.9±2.5 % for AC1, AN1, and AN4. Fractured surfaces (not included in the report) revealed the pores in the PZ to be filled with residual boria glass. The PZ merged into a continuous DZ, which had a chemical composition of ~35.24 at% zirconium and ~7.44 at% niobium (Spec. 8). A porosity of 4.3±2.3 % and 3.5±1.8 % was calculated for the DZ of AN1 and AN4 . Since AC1 did not form a distinct DZ, the amount of porosity could not be calculated. A niobium-rich oxide phase with the chemical composition of 5.82 at% zirconium, 70.09 at% and niobium separated the MZ and the PZ of AN1 specimens at thinnest oxide scale (Spec. 4). A DZ was not formed in these regions. Cross-sections of AN4 specimens revealed a similar niobium-rich phase at thinnest oxide scale thickness. The phase appeared between the MZ and DZ and had a chemical composition of 8.12 at% zirconium and 69.13 at% niobium (Spec. 9). The porosity inside the top most MZ was calculated as 7.9±5.1 %, 10.3±5.6 %, and 5.3±4.8 % for AC1, AN1, and AN4. According to EDS mappings (not included in the report), the MZ consisted of zirconium-rich grains and a continuous niobium-rich phase. A gradient of zirconium was identified inside the niobium-rich phase with 4.92 at% zirconium at the surface to 2.50 at% at the bottom of the MZ (Spec. 1 and Spec. 2). The zirconium-rich oxide grains of AN1 specimens revealed a composition of 32.10 at% zirconium and 4.12 at% niobium (Spec. 3), whereas the zirconium-rich grains of AN4 specimens showed a composition of 35.22 at% zirconium and 7.33 at% of niobium (Spec. 6 and Spec. 7). Furthermore, the size of the grains inside the MZ increased with respect to time from 3.1±2.8 µm to 10.2±4.3 µm. Fig. 6b clearly shows differences in coloration inside the zirconia-rich grains inside the niobium-rich phase. Whereas the core appears dark, a surrounding outer layer appears bright, which indicates a shell structure around the grains (marked in Fig. 6b). Fig. 7 shows the results of the TEManalysis, which was used to characterize the core-shell structure. A HAADF-STEM micrograph with EDS spot-analysis is shown in Fig. 7a. The TEM-lamella revealed the core-shell structure of the zirconia-rich grains inside the MZ. According to the EDS spot-analysis, the core consists of 88.3 at% zirconium and 10.1 at% niobium (Spec. 10). However, the diffractogram of that phase indicates monoclinic zirconia (m-ZrO₂) (Fig. 7b). The outer part of the grains transformed to a continuous shell around the zirconia core, had a thickness of ~500 nm, and a chemical composition of 72.1 at% zirconium and 26.8 at% niobium (Spec. 11). The diffractogram presents a not commensurable lattice with characteristic approximants (blue circles) beside the main intensities, which indicated the modulated crystal structure of the solid solution $Nb_2Zr_6O_{17}$ (Fig. 7c) [15]. A chemical composition of 5.4 at% zirconium, 90.3 at% niobium and impurities of 3.9 at% titanium was measured by means of EDS spot-analysis for the niobium-rich phase (Spec. 12). The diffractogram (not in the report) shows a complex structure, which was not assignable to a distinct crystal phase.

3.4 | OXIDATION KINETICS

Fig. 9 summarizes the results of the oxide scale thickness measurements of all tested specimens with calculated standard deviation. Two qualitative trends can be seen from the data. First, Nb-coated ZrB_2 showed a reduced thickness for the PZ compared to uncoated ZrB_2 (UC). Second, the homogeneity of the oxide scale thickness increased for Nb-coated ZrB_2 , which is represented by the reduced standard deviation of the calculated oxide layer thicknesses. The PZ of UC1 and UC4 had a thickness of $176\pm41~\mu m$ and $312\pm58~\mu m$, whereas AC1, AN1, and AN4 formed an average thickness of $166\pm12~\mu m$, $45\pm14~\mu m$, and $74\pm15~\mu m$ (Fig. 8a). The squares of thickness as a function of oxidation time were plotted for UC and AN specimens. UC specimens followed parabolic oxidation kinetics at $1500~^{\circ}C$. AN specimens followed that parabolic trend with reduced curvature (Fig. 8b). The squares of thickness of the single sub-layers of AN specimens are shown in a separate plot. All sublayers of AN specimens followed a parabolic growth rate and the thickness of the reaction zone (RZ = DZ + MZ) was always thicker than the PZ (Fig. 9c).

4 | DISCUSSION

It is well known, ZrB₂ oxidizes to form liquid B₂O₃ with a melting point of 450 °C and porous ZrO₂ with columnar outer zirconia and inner equiaxial porous zirconia [1, 5]. The addition of Nb and other transition metals improves the oxidation behavior as mentioned in the literature [1, 11, 12]. The results of the current study showed an improvement of the oxidation resistance by means of Nb-coatings, forming a protective RZ as a top most layer. The need for annealing, the influence of the coating to the surface coverage, the scale morphology and kinetics will be discussed.

4.1. SURFACE COVERAGE

Liquid boria glass acts like a diffusion barrier against oxygen and prevents further oxidation as long as it remains on top of the surface of ZrB₂. Consequently, it promotes controlled oxidation kinetics [5, 6]. Several studies have also confirmed the beneficial functionality of borosilicate glass oxidation layers produced by adding SiC into ZrB₂, since boria has a vapor pressure of 233 Pa at 1500 °C, whereas silica has a vapor pressure of 3x10⁻⁴ Pa [22-26]. However, borosilicate glass accumulates and leads to an uneven coverage during initial oxidation stages and

imperfections like burst bubbles due to the formation of gas components inside the glass. The current study revealed that the reaction of the deposited Nb-coating and the formed boria led to an extensive surface wetting and intact glassy scale. [27]. Previous studies observed a p-type oxidation of Nb, which undergoes different oxidation stages with respect to the temperature and time from NbO, T-Nb₂O₅, and B-Nb₂O₅, to monoclinic H-Nb₂O₅ [28-33]. According to phase diagrams, Nb₂O₅ has its melting point at 1479 °C and is completely miscible with B₂O₃ at 1485 °C, whereas the solubility of zirconia in boria is limited up to 12 mol% [14, 16, 17, 26, 34]. During cooling niobia precipitates within the super saturated liquid solution. XRD diffraction patterns of Nb-coated specimens showed the presence of orthorhombic ammonium pentaborate tetrahydrate B₅H₁₂NO₁₂, which forms during storing B₂O₃ in humid ambient air and proves the presence of boria at the surface after oxidation (see Fig. 4). With increased oxidation time the intensity of the peaks for the boria phase decreases, which indicates loss of the boria scale with time [35]. In the current study, the calculated coverage of protective glassy boria had been seen in the order of UC1 (30 %) < AC1 (52 %) < AN4 (62 %) < AN1 (99 %) and showed an identical tendency. Therefore, it is believed that the liquid solution of Nb₂O₅ and boria has a lower vapor pressure than pure boria and led to a thick and continuous coverage with a protective liquid glass for longer exposure times. Similar results had been reported in previous papers by adding 6 mol% Nb into the ZrB₂-matrix. Dehdashti et al observed the formation of a two-layer oxide scale, consisting of a glassy outer scale of B₂O₃ with dissolved Nb and Zr as well as a porous zirconia oxide scale within the solid solution Nb₂Zr₆O₁₇. The liquid solution of B₂O₃ with Nb₂O₅ increased the stability of the glass by reducing its vapor pressure and improved the oxidation resistance of the underlying compound [11, 12].

4.3. OXIDE GRAIN MORPHOLOGY

AC1 has shown large arbitrary shaped grains with few engraved micro structured areas on top of the oxidized surface (see Fig. 1c). The chemical composition of these engraved areas indicated a mixture of ZrO₂ and niobia. Short term oxidation experiments of AC specimens (not included in this report) have shown that the formation of liquid boria beneath the coating caused spallation. Residual niobia flakes, which were floating in the glass, might have reacted with the zirconia grains during longer exposure times and would have formed the arbitrary grains with engraved micro structures. Similar oxide grain morphology at the surface was found near the edges of annealed specimens after oxidation. Cross-sections revealed the absence of the coating at these spots due to local spallation during oxidation. Therefore, arbitrary shaped grains on top of the boria glass indicate the failure of the adhesion of the coating, whereas smooth and globular zirconia grains on top of the glassy boria indicate an intact adhesion of the coating.

Polished cross-sections of AN4 specimens revealed the formation of mixed oxide grains, which were bonded to the MZ (see Fig. 6c). It is hypothesized that globular and smooth zirconia grains on top of the liquid boria grew in size inside the boria glass with respect to the time due to sintering effects and finally sank into the underlying niobia layer. The zirconia grains reacted with the niobia to form mixed oxides, formed a core-shell structure with a monoclinic core and a reacted micro structured surface, and bonded to the niobia-covered surface. SEM micrographs as well as XRD- and TEM-diffraction have proven the formation of the mixed oxide phase Nb₂Zr₆O₁₇ around monoclinic zirconia grains near and inside the MZ (see. Fig. 4, Fig. 6b, Fig. 7a-c) [15-17, 19].

4.4. OXIDE SCALE MORPHOLOGY

Nb-coated ZrB₂ promotes the formation of a multilayer oxide scale with increased density (see Fig. 5b-c). The schematic in Fig. 9 describes the oxide scale evolution of annealed Nb-coated ZrB₂ during oxidation at 1500 °C with respect to the time. The IDZ prevented detachment during oxidation and led to the p-type oxidation of Nb to NbO (T_{melt} 1915 °C) and NbO₂ near the interface zone as well as Nb₂O₅ (T_{melt} 1479 °C) at the surface, which was proven by EDS spotanalysis (see Fig 6, Spec. 4) [14, 28, 36]. Since niobium and niobia do not prevent oxidation diffusion, ZrB2 formed an oxidation front of liquid boria and columnar porous zirconia beneath the coating. Liquid Nb₂O₅ forms with respect to the time at 1500 °C and led to the infiltration of the porous zirconia by liquid niobia. Both oxides, liquid Nb₂O₅ and solid ZrO₂, reacted with each other and formed a solid solution and liquid solution (see Fig. 6c) [14]. BSE cross-sectional micrographs and TEM diffraction proved that zirconia grains reacted with the circulating liquid niobia and formed a core-shell structure with a monoclinic ZrO₂-core and a shell of Nb₂Zr₆O₁₇ (see Fig. 6b and Fig. 7a-c). The size of the grains inside the MZ increased with respect to the time from 3.1±2.8 µm to 10.2±4.3 µm and therefore, the porosity of the MZ decreased from 10.3 ± 5.6 % to 5.3 ± 4.8 %. Further infiltration and densification due to liquid phase sintering led to the formation of a DZ with a porosity of 3.5 \pm 1.8 %. EDS spot-analysis proved that the chemical composition of the reacted zirconia grains inside the MZ are approaching the chemical composition of the densified DZ with respect to the time. Therefore, it can be assumed that the mixed oxide shells around the zirconia grains grow with time by consuming the inner core of pure monoclinic zirconia to form a zirconia-based solid solution with a composition of ~90 at% zirconium and ~10 at% niobium (see. Fig. 6c, Spec 6, Spec. 8). A similar mechanism was reported by Zhang et al [9]. The addition of tungsten carbide led to the formation of WO₃-liquid inside the oxide scale. Liquid phase sintering effected the zirconia grains and increased the density of the oxide scale as long as the liquid remains. Most of the WO₃-liquid evaporated before

complete densification due to its reinforced volatility above 1300 °C. The more thermally stable boria liquid solution of niobia and boria remained on top of the surface even after 4h of oxidation and protected the underlying liquid niobia against evaporation. Therefore, the density and thickness of the DZ and MZ increased with respect to the oxidation time.

4.5. SCALE THICKNESS AND OXIDATION KINETIC

As long as a continuous layer of boria is present on top of ZrB₂, the oxidation rate follows parabolic law [27]. The porous zirconia scale offers no protection against oxygen diffusion. However, a dense oxide scale is preferable to reduce the inward diffusion of oxygen to the reaction front, according to the model of ZrB2-oxidation of Parthasarathy et al [5, 6]. Decreased porosity reduces the oxidation rate constants and oxide scale thickness. Similar results were shown in this study. The formation of a protective and dense RZ due to the reaction of the oxide products of the annealed Nb-coating and ZrB2 reduced the parabolic oxidation kinetics (see Fig. 8b). Measurements of the total oxide scale thickness after 4h of oxidation revealed a reduction in total scale thickness by 50 %. In particular, the thickness of PZ was reduced by 76 % for AN4 specimens (74 μm) compared to baseline ZrB₂ UC4 (312 μm). AC specimens were not able to improve the oxidation behavior, since the coating spalled during oxidation. Compared to that, Dedashtie et al reported an improvement of 40 % after 3h of oxidation at 1500°C due to the addition of 6 mol% Nb. A densification was not investigated. The improvement was attributed to the increased coverage of glassy boria [11, 12]. In contrast to that, the solid and protective RZ at the surface of Nb-coated and annealed specimens follows a parabolic growth rate and controls the oxygen diffusion as well as the oxidation kinetics of ZrB₂ (see Fig. 8c). From the data it can be seen, as long as the thickness of the RZ is higher than the PZ (ratio RZ/PZ > 1), that the overlying RZ is protective against further oxidation. For example, AN1 shows a ratio of 1.06 $(48 \mu m \text{ to } 45 \mu m)$, AN4 a ratio of 1.11 $(82 \mu m \text{ to } 74 \mu m)$ and AC1 a ratio of 0.12 $(20 \mu m \text{ to } 1.11 \mu m)$ 166 µm). Recapitulatory, the MZ gets protected by the liquid boria solution for longer times and increases the thickness and density of the RZ due to liquid phase sintering of mixed oxide grains and controls the oxidation kinetics even when the liquid boria evaporated completely (see Fig. 8c).

5 | CONCLUSIONS

Following conclusions can be drawn from this study:

Magnetron sputtering is a successful method to deposit metallic Nb-coatings on ZrB₂.

- The formation of a liquid boria solution with liquid Nb₂O₅ increased the stability of the protective glass at the surface and the surface coverage up to 62 % after 4h of oxidation.
- Annealed Nb-coatings led to a multilayer oxide scale morphology with a mixed zone
 (MZ) at the top, intermediate dense zone (DZ) and inner most porous zirconia zone (PZ).
- The MZ and DZ showed a reduced porosity of 5.3±4.8 % and 3.5±1.8 % compared to the PZ with a porosity of 6.9±2.5 % after oxidation of 4h at 1500 °C.
- The protective reaction zone (RZ = MZ + DZ) followed a parabolic growth rate, controlled the parabolic oxidation kinetics of ZrB_2 , and reduced the thickness of the PZ by 76 %
- Oxidation protection is guaranteed for 4h at 1500 °C due to a dense and solid RZ.

ACKNOWLEDGMENTS

UHTC-Group at Missouri S&T for the support of materials for extreme environments.

Luis Baier and Felix Vogel (DLR Stuttgart) for the annealing.

Dr. Peter Mechnich for his assistance in oxidation experiments.

Dr. Kelm and Frederik Kreps for preparing and analyzing the TEM-lamella.

Cynthia Yanel Guijosa Garcia and Alexander Francke for the assistance in XRD analyzing.

REFERENCES

- 1. Fahrenholtz, W.G. and G.E. Hilmas, *Oxidation of ultra-high temperature transition metal diboride ceramics*. International Materials Reviews, 2012. **57**(1): p. 61-72.
- 2. Guo, W.-M., et al., Effects of Re_2O_3 addition in hot-pressed ZrB_2 -SiC ceramics. Journal of the European Ceramic Society, 2009. **29**: p. 3063-3068.
- 3. Inoue, R., et al., *Oxidation of ZrB2 and its composites: a review.* Journal of Materials Science, 2018. **53**: p. 14885-14906.
- 4. Fahrenholtz, W.G., *The ZrB*₂ *Volatility Diagram*. Journal of The American Ceramic Society, 2005. **88**(12): p. 3509-3512.
- 5. Parthasarathy, T.A., et al., *A model of the oxidation of ZrB*₂, *HfB*₂ and *TiB*₂. Acta Materialia, 2007. **55**: p. 5999-6010.
- 6. Parthasarathy, T.A., Effects of Phase Chenge ond Oxygen Permeability in Oxide Scales on Oxidation Kinetics of ZrB2 and HfB2. Journal of The American Ceramic Society, 2009. **92**(5): p. 1079-1086.
- 7. Cissel, K.S. and E. Opila, *Oxygen diffusion mechanisms during high-temperature oxidation of ZrB2-SiC*. Journal of The American Ceramic Society, 2018. **101**: p. 1765-1779.
- 8. Paul, A., et al., *UHTC composites for hypersonic applications*. American Ceramic Society Bulletin, 2012. **91**(1): p. 22-29.

- 9. Zhang, S.C., G.E. Hilmas, and W.G. Fahrenholtz, *Improved Oxidation Resistance of Zirconium Diboride by Tungsten Carbide Additions*. Journal of The American Ceramic Society, 2008. **91**(11): p. 3530-3535.
- 10. Hu, P., et al., Effect of Various Additives on the Oxidation Behavior of ZrB2-Based Ultra-High-Temperature Ceramics at 1800°C. Journal of The American Ceramic Society, 2010. **93**(2): p. 345-349.
- 11. Dehdashti, M.K., W.G. Fahrenholtz, and G.E. Hilmas, *Oxidation of zirconium diboride with niobium additions*. Journal of the European Ceramic Society, 2013. **33**: p. 1591-1598.
- 12. Dehdashti, M.K., W.G. Fahrenholtz, and G.E. Hilmas, *Effects of transition metals on the oxidation behavior of ZrB*₂ *ceramics*. Corrosion Science, 2015. **91**: p. 224-231.
- 13. Dehdashti, M.K., W.G. Fahrenholtz, and G.E. Hilmas, *Effects of temperature and the incorporation of W on the oxidation of ZrB*₂ *ceramics*. Corrosion Science, 2014. **80**: p. 221-228.
- 14. Wang, F. and D.O. Nothwood, *Oxides formed between ZrO₂ and Nb₂O₅*. Journal of Materials Science, 1995. **30**: p. 4003-4008.
- 15. Galy, J.R., R. S., *The Cyrstal Structre of Nb2Zr6O17*. Journal of Solid State Chemistry, 1973. **7**: p. 277-285.
- 16. Mestres, L., O. Martínez-Sarrión, and J. Fernández-Urbán, *Phase Diagram at Low Temperature of the System ZrO*₂/*Nb*₂*O*₅. Zeitschrift für anorganische und allgemeine Chemie, 2000(627): p. 294-298.
- 17. Roth, R.S. and L.W. Coughanour, *Phase Equilibrium Relations in the Systems Titania-Niobia and Zirconia-Niobia*. Journal of research of the National Bureau of Standards, 1955. **55**(4): p. 209-213.
- 18. Thompson, J.G.W., R. L.; Sellar, J.; Barlow, P. J.; Hyde, B. G., *Incommensurate Composite Modulated Nb2Zrx-2O2x+1*. Journal of Solid State Chemistry, 1990. **88**: p. 465-475.
- 19. German, R.M.S., Pavan; Park, Seong Jin, *Review: Liquid phase sintering*. Journal of Materials Science, 2009. **44**: p. 1-39.
- 20. Nelson, E.S.C., Phillip, Parametric Study of Reactive Melt Infiltration. 2000.
- 21. Neuman, E.W.H., Gregory E.; Fahrenholtz, William G., *Processing, microstructure, and mechanical properties of large-grained zirconium diboride ceramics*. Materials Science and Engineering: A, 2016. **670**: p. 196-204.
- 22. Shugart, K. and E. Opila, *SiC Depletion in ZrB*₂-30 vol% *SiC at Ultrahigh Temperatres*. Journal of The American Ceramic Society, 2015. **98**(5): p. 1673-1683.
- 23. Shugart, K., et al., *Mechanisms of Variability of ZrB*₂-30 vol% SiC Oxidation Kinetics. Journal of The American Ceramic Society, 2014. **97**(7): p. 2279-2285.
- 24. Shugart, K., W. Jennings, and E. Opila, *Initial Stages of ZrB*₂-30 vol% SiC Oxidation at 1500°C. Journal of The American Ceramic Society, 2014. **97**(5): p. 1645-1651.
- 25. Shugart, K., et al., *Determination of Retained B2O3 Contet in ZrB*₂-30 vol% SiC Oxide Scales. Journal of The American Ceramic Society, 2015. **98**(1): p. 287-295.
- 26. Karlsdottir, S.N. and J.W. Halloran, *Zirconia Transport by Liquid Convection during Oxidation of Zirconium Diboride-Silicon Carbide*. Journal of The American Ceramic Society, 2008. **91**(1): p. 272-277.

- 27. Naraparaju, R., et al., *Effect of moisture on the oxidation behaviour of ZrB*₂. Journal of The American Ceramic Society, 2019. **104**(2): p. 1058-1066.
- 28. Nico, C., et al., *NbO/Nb₂O₅ core-shells by thermal oxidation*. Journal of the European Ceramic Society, 2013. **33**: p. 3077-3083.
- 29. Bouillet, C., et al., *Oxidation of niobium sheets at high temperature*. Solid State Ionics, 1997: p. 819-824.
- 30. Vishwanadh, B., et al., *A Study on the Oxidation Behavior of Nb Alloy (Nb-1 pct Zr-0.1 pct C) and Silicide-Coated Nb Alloys.* The Minerals, Metals & Materials Society, 2012. **44A**: p. 2258-2269.
- 31. Kofstad, P. and H. Kjollesdal, *Oxidation of Niobium (Columbium) in the Temperatue range 500°C to 1200°C*. Transition Metal Society AIME, 1961. **221**.
- 32. Kofstad, P., *High Temperature Oxidation of Metals*. Materials and Corrosion, 1967. **18**(10): p. 956-957.
- 33. Arbuzov, M.P. and V.G. Chuprina, *The Oxidation of Niobium and the Structure of Niobium Oxides*. 1965. p. 129-133.
- 34. Levin, E.M., *Phase Equilibria in the System Niobium Pentoxide -- Boric Acis*. Journal of research of the National Bureau of Standards, 1965. **70A**(1).
- 35. Morris, M.C.M., Howard F.; Evans, Eloise H.; Paretzkin, Boris, *Standard X-Ray Diffraction Poweder Patterns, Section 17 Data for 54 Substances.* 1980, Washington: U.S. Government printing office.
- 36. Nico, C., T. Monteiro, and M.P.F. Graca, *Niobium oxides and niobates physical properties: Review and prospects.* Progress in Materials Science, 2016. **80**: p. 1-37.

Table 1 Nomenclature of specimens and experimental matrix					
Specimens	Nomenclature		Annealing process	Oxidation time	Oxidation Process
Un-coated	UC	UC1		1h	1500 °C
		UC4		4h	
As-coated	AC	AC1	-	1h	Synthetic air (SA) 0.4 L/min
1h + 3h annealed	AN	AN1	1h at 1800 °C +	1h	
		AN4	3h at 1750 °C	4h	

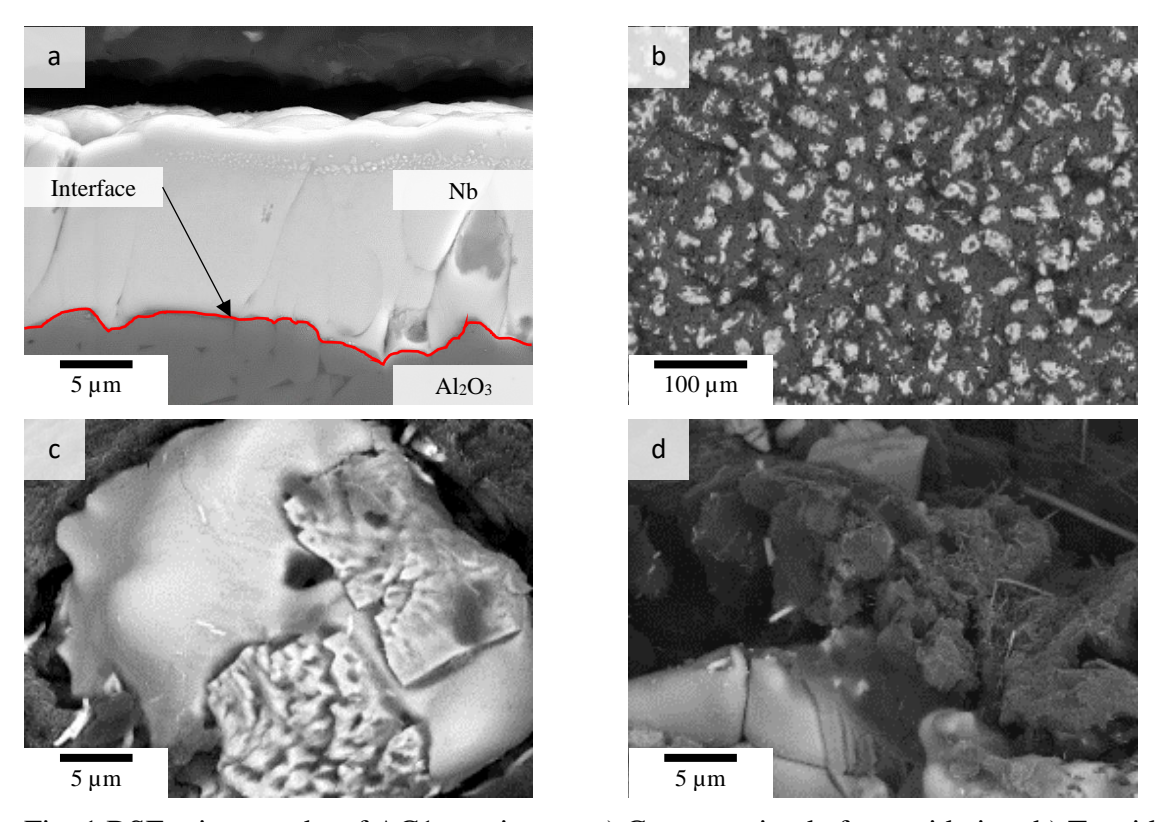


Fig. 1 BSE micrographs of AC1 specimens: a) Cross-section before oxidation, b) Topside of oxidized surface, c) Oxide grains on surface, and d) Fractured surface after 1h at 1500°C

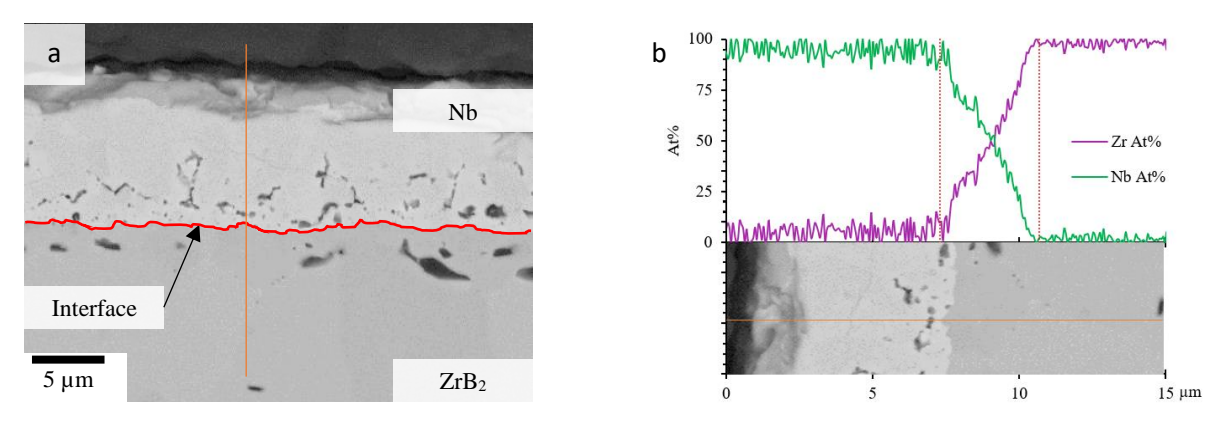


Fig. 2 BSE cross-sectional micrographs of AN specimens: a) Cross-section of the interface, b) EDS line-scan of the interface

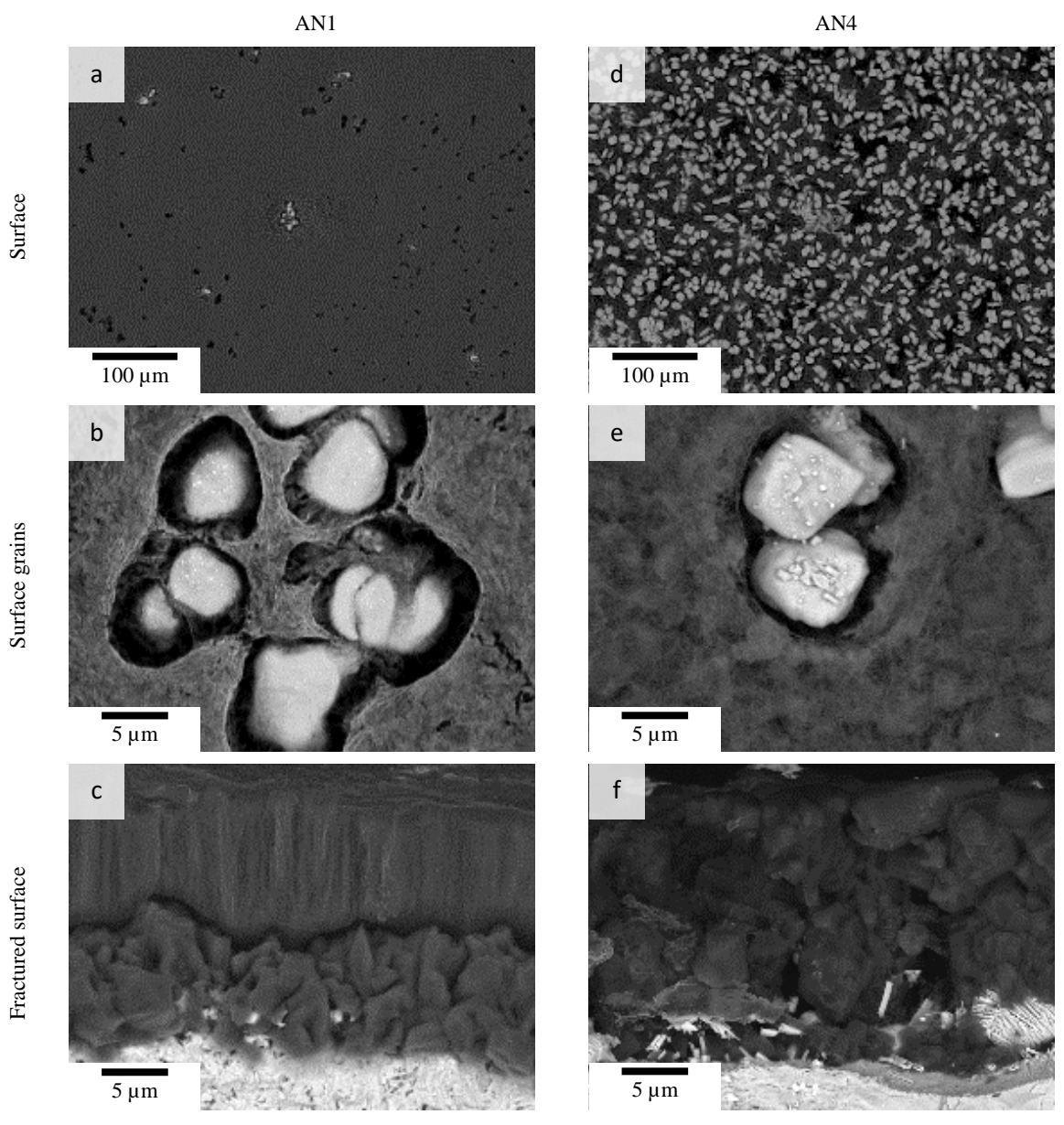


Fig. 3 BSE micrographs of the surface topside and fractured surface of oxidized specimens at $1500\,^{\circ}\text{C}$: a) AN1 and b) AN4

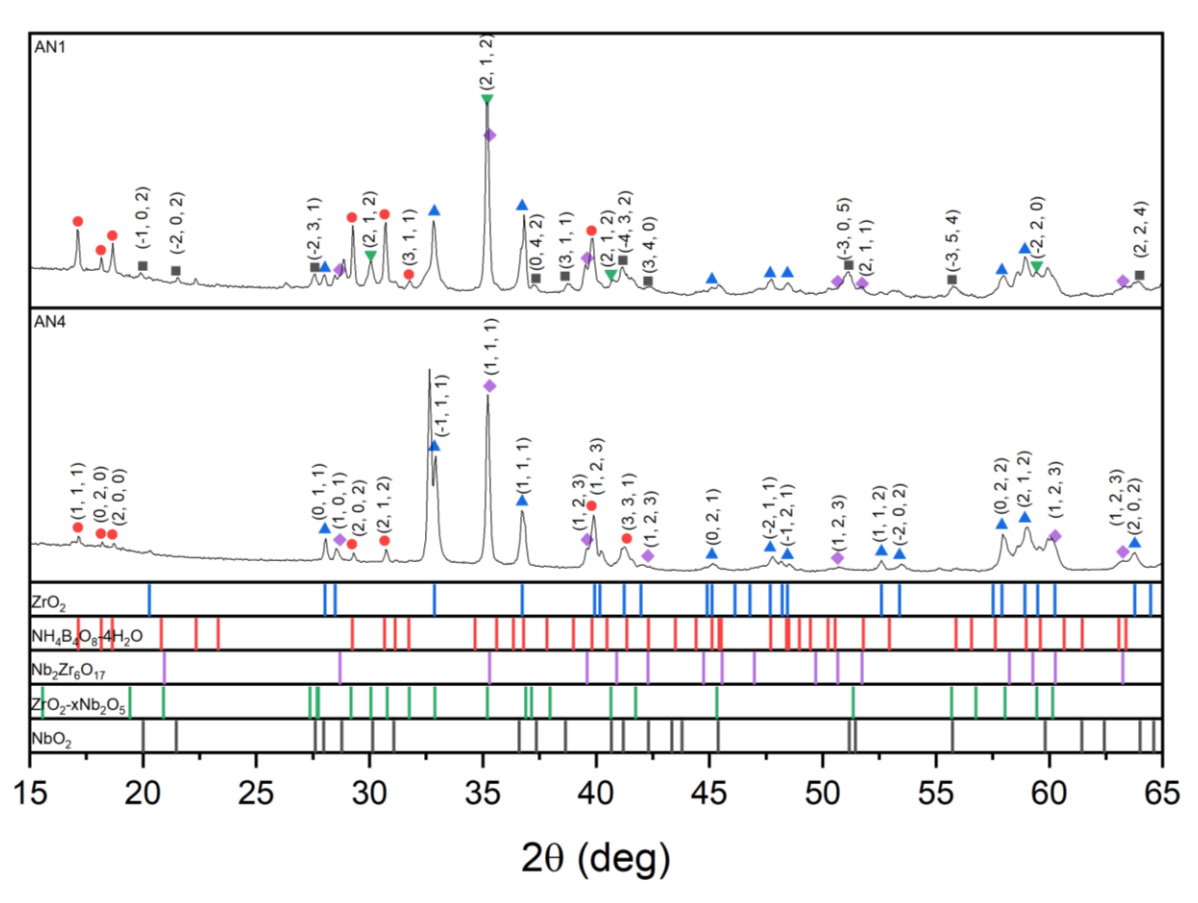


Fig. 4 X-Ray diffraction pattern for AN1 and AN4 specimens

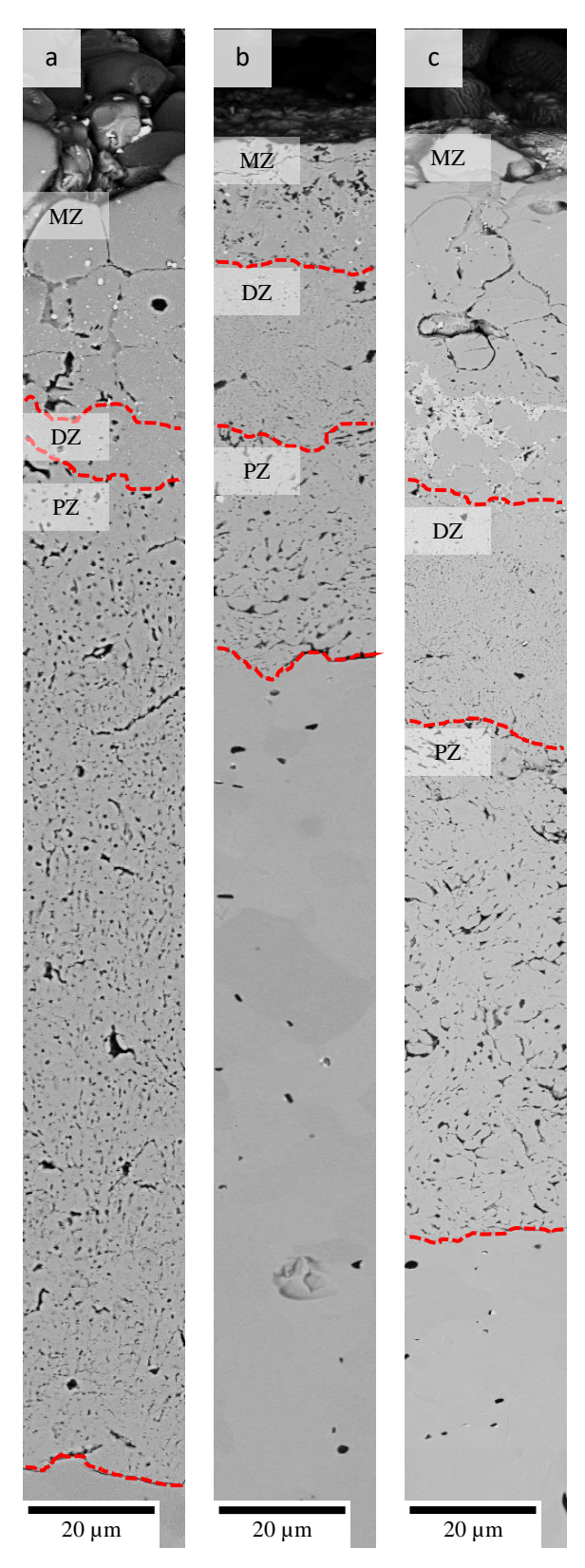


Fig. 5 BSE cross-sectional micrographs of oxidized specimens at 1500 °C with marked sub-layers: a) AC1, b) AN1, c) AN4

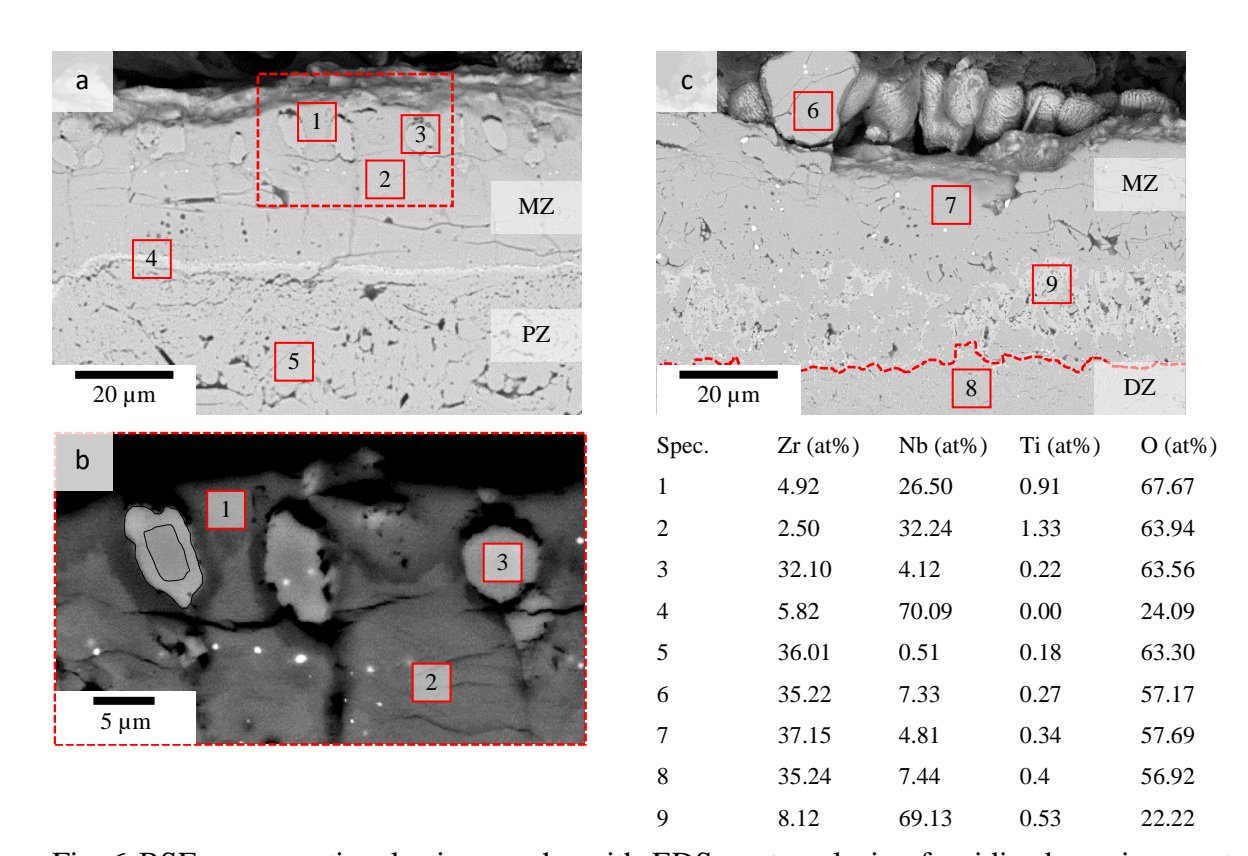


Fig. 6 BSE cross-sectional micrographs with EDS spot-analysis of oxidized specimens at 1500 °C: a) AN1, b) magnified section of AN1 (30kV), c) AN4

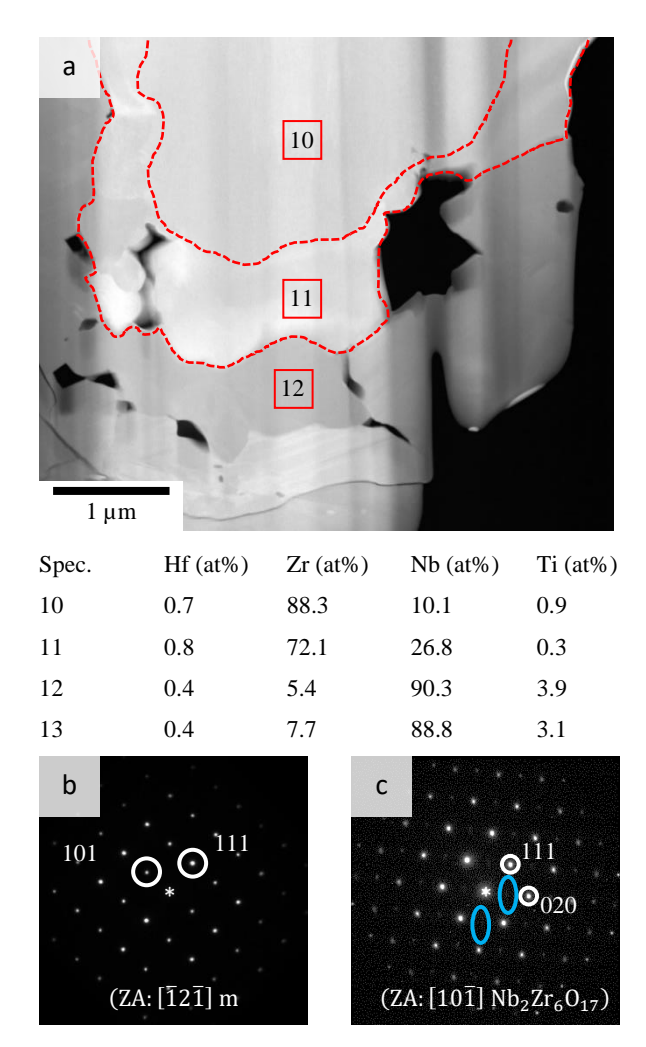


Fig. 7 a) HAADF-STEM micrograph of ZrO₂ grains inside the MZ of AN1 specimens, b) Diffractogram of spec. 10 (grain-core), c) Diffractogram of spec. 11 (outer-shell)

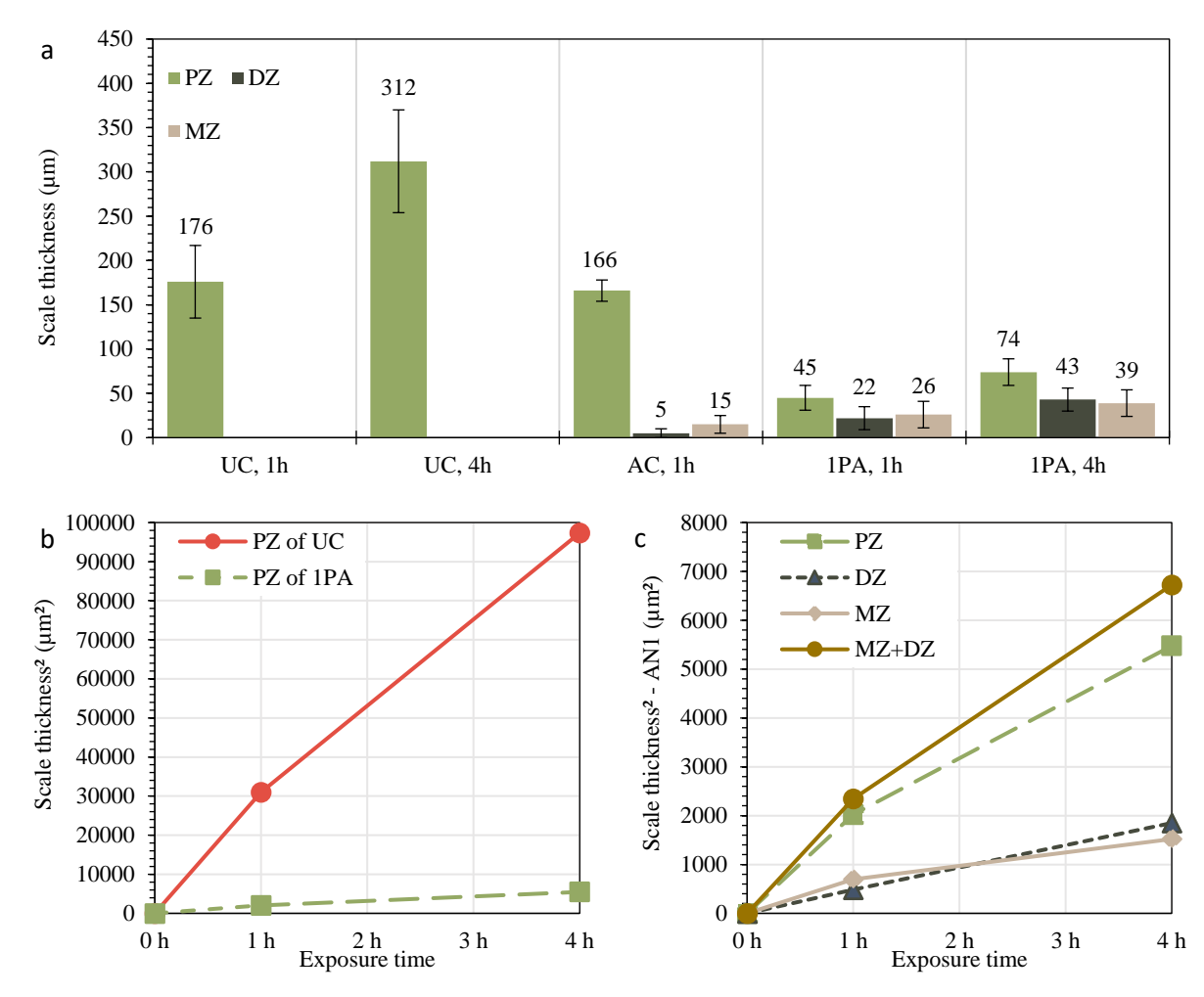


Fig. 8 a) Measured oxide scale thicknesses at 1500 °C; b) Squares of the thickness of the PZ with respect to the time; c) Squares of AN1 sub-layer thickness with respect to the time.

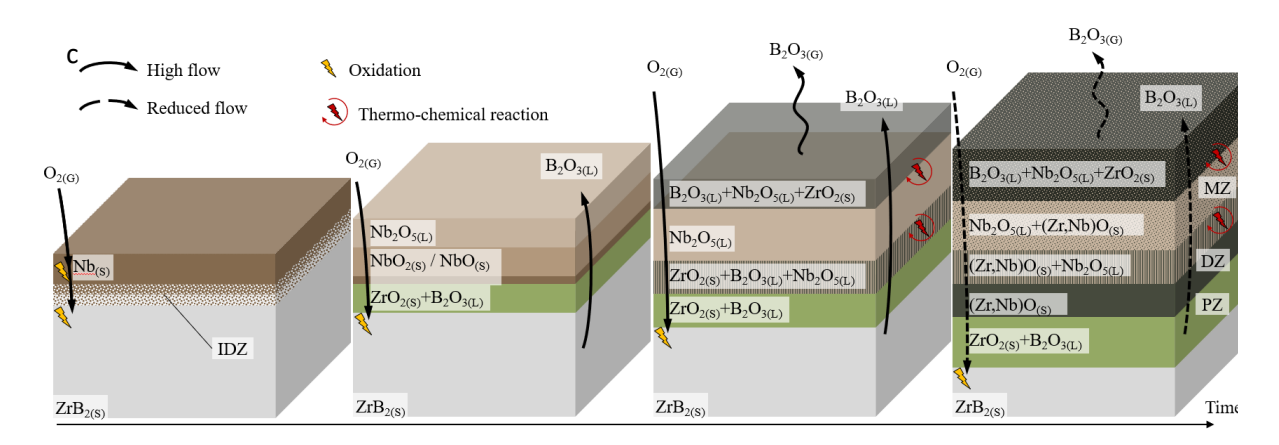


Fig. 9 Oxide scale formation of annealed Nb-coated ZrB₂ at 1500 °C with respect to time.